

Exhibiting environment sensitive optical properties through multiscale modelling: A study of photoactivatable probes

Peer-reviewed author version

Osella, S.; Marczak, M; Murugan, N. Arul & KNIPPENBERG, Stefan (2022)

Exhibiting environment sensitive optical properties through multiscale modelling: A study of photoactivatable probes. In: Journal of Photochemistry and Photobiology A-chemistry 425 (Art N° 113672).

DOI: [10.1016/j.jphotochem.2021.113672](https://doi.org/10.1016/j.jphotochem.2021.113672)

Handle: <http://hdl.handle.net/1942/36484>

Exhibiting environment sensitive optical properties through multiscale modelling: a study of photoactivatable probes

S. Osella^{1*}, M. Marczak¹, N. Arul Murugan², S. Knippenberg^{3,4,5*}

1. Chemical and Biological Systems Simulation Lab, Centre of New Technologies, University of Warsaw, Banacha 2C, 02-097 Warsaw, Poland;
2. Department of Computer Science, School of Electrical Engineering Science and Computer Science, KTH Royal Institute of Technology, SE-10044 Stockholm, Sweden;
3. Department of Theoretical Chemistry and Biology, School of Engineering Sciences in Chemistry, Biotechnology and Health, KTH Royal Institute of Technology, SE-10691 Stockholm, Sweden
4. Regional Centre of Advanced Technologies and Materials, Czech Advanced Technologies and Research Institute, Palacký University Olomouc, Křížkovského 8, Olomouc 779 00, Czech Republic;
5. UHasselt, Theory Lab, Agoralaan, 3590 Diepenbeek, Belgium.

* Correspondence: s.osella@cent.uw.edu.pl; stefan.knippenberg@uhasselt.be

Abstract

To assess a tumor biomarker like the cyclooxygenase-2 enzyme (COX-2), non-invasive imaging techniques are powerful tools. The (non-) linear optical properties of activatable fluorescent probes which are selectively bound to the biomarker can therefore be exploited. The here presented molecular modelling results based on multi-scale modelling techniques highlight the importance of the conformational versatility and of changes in the electronic interactions of such probes when they are embedded in water or in the COX-2 homodimer enzyme. The ANQ-IMC-6 probe, which combines the binding domain/scaffold of indomethacin (IMC) on COX-2 with the optical properties of acenaphtho[1,2-b]quinoxaline (ANQ), is found to be folded in the solvent and unfolded in the enzyme. A concerted movement of the probe and the protein is seen, while the rotational autocorrelation function exhibits also the intrinsic properties of the probe. Hybrid Quantum Mechanics/Molecular Mechanics (QM/MM) calculations are used to simulate the one-photon and two-photon absorption spectra along with the first hyperpolarizability. The transition has a local character in vacuum, but changes to a charge transfer one in the presence of the microenvironment of the enzyme. This is also visible through a change of the shape of the absorption spectrum, while at the same time the simulated signals of second harmonic generation experiments are strongly enhanced. The results of this work prove that an environment sensitive probe with an anchoring group and an optical active part can be constructed for use in absorption spectroscopy, without the need to revert to fluorescence experiments.

Keywords: Biomarker, cancer, multiscale modeling, QM/MM, conformational change, optical properties

Introduction

Cyclooxygenase (COX) is an enzyme of the prostaglandin-endoperoxide synthase family, which is found in two isomers, COX-1 and COX-2 and plays a crucial role in the formation of prostanoids.¹ In particular, high levels of COX-2 have been found in pancreatic, gastric, breast, stomach, and colon carcinoma, as well as in inflammatory lesions.²⁻¹⁰ As a result, COX-2 is considered as a very promising biomarker for the detection of tumours¹¹⁻¹⁶ and its presence can reveal important information for cancer treatment. To assess the presence of COX-2, fluorescent probes are used which provide the diagnosis via non-invasive and high-resolution real time imaging techniques. This fluorescence detection has been used to visualize cells in vivo and in vitro, and is a very powerful tool both for biological research and clinical screening.

Driven by a dire need, in the last decades different fluorescence-based probes for the specific target of COX-2 have been designed and tested¹⁷⁻²³ but their application for clinical use still needs to be evaluated. Generally, these probes can be divided into two families: the active and activatable probes.²⁴ The latter ones are based on an 'off/on' mechanism, while the former work by conjugating the fluorophore and the inhibitor to selectively bind to COX-2, which leads to the strong enhancement of the emission due to the accumulation of the probe in the enzyme as contrast agent. In contrast, the activatable probes are inherently weakly fluorescent due to intramolecular charge transfer, energy transfer or photon induced electron transfer (PET) mechanisms. They can act as a trigger since they become strongly fluorescent after binding to COX-2. However, in order to differentiate between COX-2 and COX-1, the selectivity of the probe has to be enhanced. It can be achieved by tuning specific interactions with the active sites of the enzyme, acting as inhibitors, as well as to modify the structure of the probe itself through conjugation with fluorescent dyes.²⁵⁻
²⁸ The COX-2 enzyme is a most suited target for diagnostic purposes thanks to its role as up-regulator for cancer, but the strong structural similarities with COX-1 are problematic. In fact, 84% of the isoenzymes are similar and active sites with more than 90% homology have been observed.^{29,30} It might be detrimental for the clinical use of these systems as the acquired accuracy is limited by the availability of only a few selective binding sites.³¹ As a result, indomethacin (IMC) as inhibitor can interact with both isoenzymes³², but while COX-2 is found in malignant cells, COX-1 is mainly expressed in healthy tissues and it can lead to misdiagnosis. Therefore, further effort in tuning the probe specificity is requested.

One promising candidate is the ANQ-IMC-6 probe (Figure 1), composed of two subunits connected via a six atoms carbon aliphatic linker, namely the IMC and acenaphtho[1,2-b]quinoxaline (ANQ). In this probe, IMC acts as the binding domain upon COX-2 interaction while ANQ carries the fluorescent properties which enables the imaging. As it is based on IMC, this probe presents the ‘off/on’ mechanism described above, which depends on the conformation the probe can adopt in different environments. In fact, in its free state ANQ-IMC-6 adopts a folded conformation which is responsible for the PET leading to weak fluorescence, but when it is bound to COX-2 the geometry of the binding site forces the probe to unfold, thus hindering the PET which induces a strong fluorescence.²¹ This probe was synthesized and exhibited a very high two-photon induced fluorescence in the presence of COX-2, with cross section values up to 133 GM at 800 nm excitation, which was reported to be a 28 fold enhancement compared with that in absence of the enzyme.²² Its selectivity towards cancer cells was confirmed by in vitro imaging.

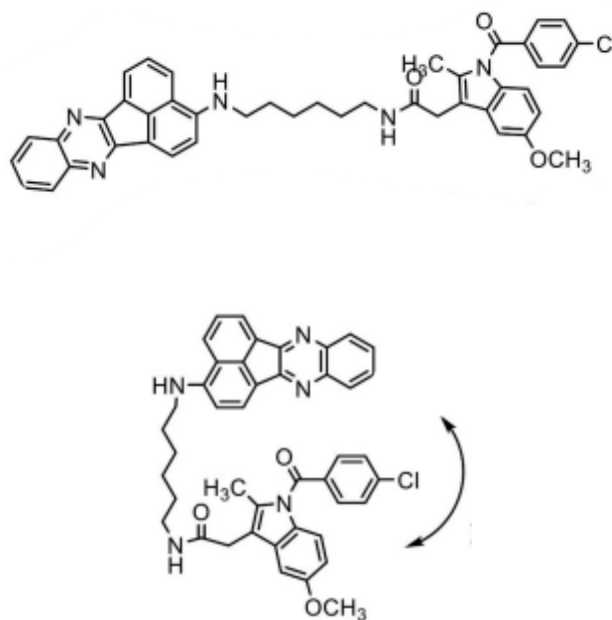


Figure 1: Unfolded (top) and folded (bottom) ANQ-IMC-6

The discrimination between cancer cells and inflammatory lesions is based on the different response of the probe due to the differing concentrations of COX-2 in the two systems. In fact, at a low concentration ($< 0.085 \mu\text{g/ml}$) as found in inflammatory lesion, COX-2 is present as a monomer and the probe fluoresces at 615 nm. In cancer cell, the enzyme is present as a homodimer due to its increased concentration ($> 0.085 \mu\text{g/ml}$) and the probe fluoresces then at 555 nm.^{33,34}

Thus, this fluorescence blue shift can be used to distinguish between the two systems. To explain the difference in selectivity based on different concentration levels of the enzyme, the following mechanism has been suggested. In inflammatory lesions where COX-2 is present as monomer, ICM binds at the interface between the protein and the water environment, leaving the ANQ fluorophore exposed to the aqueous microenvironment responsible for emission at higher wavelengths. On the other hand, in cancer cells COX-2 is present as homodimer and now the whole probe is bound to the interface of the two monomers and the ANQ moiety experiences a different, more hydrophobic microenvironment which leads to emission at lower wavelengths.^{21,24} Despite this explanation, no proof of the proposed mechanism has been found in literature up to date.

In this study, we report a multiscale computation of the ANQ-IMC-6 probe optical response when embedded in the COX-2 enzyme in order to investigate its use as a (non) linear spectroscopic compound to identify the enzyme, thus retrieving to the power of absorption properties of this probe. The current manuscript is constructed as follows. After a brief overview of the computational details, benchmark results for the molecular spectra are provided to enforce the quality of the used computational protocols based on time dependent density functional theory, which have been chosen with respect to an efficient use of the computational means. In a second part of the discussion, the focus is put on the atomistic Molecular Dynamics simulation, needed to get a view on the specific protein environment and the conformational details of the bound probe. Since in the protein only the unfolded conformation is found, further analysis is focused on this form of the probe only. Thereupon, snapshots are selected out of these trajectories and by means of hybrid Quantum Mechanics – Molecular Mechanics calculations, the (non) linear optical spectra of the probe are obtained. The one-photon, two-photon absorption spectra are analysed, as well as the first hyperpolarizability used to get access to the Second Harmonic Generation and Hyper Rayleigh Scattering of the probe embedded in the protein. Finally, the conclusions of the study are concisely given as well as the details of the computational methodology.

Computational details

To evaluate the quality of the used quantum chemical approaches, a benchmark was done using Density Functional Theory (DFT) along with the B3LYP^{35,36} and CAM-B3LYP³⁷ functionals, and Dunning's correlation consistent cc-pVDZ basis set.³⁸ By means of Gaussian16,³⁹ the geometries of both folded and unfolded conformations have been optimized, followed by a single point time

dependent density functional theory (TDDFT) calculation to obtain the absorption spectra. The importance of Grimme's third generation dispersion correction (D3) was evaluated.⁴⁰ The Algebraic Diagrammatic Construction scheme (ADC) of second order [ADC(2)],⁴¹⁻⁴³ as well as the equation-of-motion coupled cluster singles and doubles approach (EOM-CCSD)^{44,45} implemented in the Q-Chem program package⁴⁶ have been used to benchmark the lowest excited states of the probe. As a result of this analysis, the CAM-B3LYP-D functional has been selected for further use and the charges of the unfolded structure computed with the CHELPG method⁴⁷ were used for the forthcoming simulation steps.

The location and orientation of the probe in the COX-2 enzyme were obtained from docking simulations performed by means of AutoDock 4.⁴⁸ A grid of 126 x 126 x 126 Å was used with a spacing of 0.375 Å, and in total 50 Lamarckian Genetic Algorithm docking runs were completed. Afterwards, Molecular dynamics (MD) simulations have been performed on the homodimer COX-2-probe complex with the Gromacs-2018.2 software and the ff99SB forcefield.^{49,50} Since the interactions with the enzyme force the probe into the unfolded conformation, only the latter one was considered at this stage of simulation. The complex has been immersed in a 2.0x2.0x2.0 nm³ box, filled with water molecules represented by the TIP3P model and neutralized considering sodium ions. The protocol used is the following. After the molecular mechanics (MM) optimization, the system was subjected to a 100 ps long NVT simulation followed by a MD equilibration performed for 20 ns in the canonical NPT ensemble at 300 K. A final production dynamics run of 50 ns was considered for the analyses. For the different steps, LINCS constraints were considered. The Verlet cut-off scheme has been applied with a short range cut of 1.5 nm for both electrostatic and van der Waals forces. The Particle Mesh Ewald method has been used for long-range electrostatics, while a dispersion correction scheme has been used for the long-range van der Waals interactions. The Berendsen thermostat has been used with a time step of 0.1 ps and T=300K and the Parrinello-Rahman isotropic pressure coupling with a time step of 2 ps at 1 bar has been used in NPT simulations.

From the production simulation, 50 frames were extracted in the last 10 ns of simulation time, and used as input geometries for hybrid quantum mechanics / molecular mechanics (QM/MM) calculations, in which the probe is considered in the QM part and the protein and water molecules in its close contact, as well as the ions, in the MM part as point charges. Throughout this study, the DALTON16 software package was used.⁵¹ Since the absorption properties are not affected by

the presence of the empirical dispersion term employed in this study,⁵² the one and two-photon absorption properties were obtained at the CAM-B3LYP/TZVP level of theory. The teams of Loos and Jacquemin assessed the accuracy of CAM-B3LYP to second order correlated methods and found an outstanding performance of this functional with respect to transition and excited state dipole moments,⁵³ which are of utmost importance in the calculation of non-linear optical spectroscopies. This functional has furtheron been benchmarked against post-Hartree–Fock methods and other density functionals in our study on the interpretation of non-linear optical and fluorescence experiments in lipid bilayer membranes performed by means of the Laurdan probe.⁵⁴ Its accuracy is also proven for other optically active probes embedded in a lipid bilayer.^{55–58}

Results and discussion

1. Benchmark

The presence of the dispersion correction term in the description of the DFT functional has been found to be essential to obtain the folded structure, while little or no differences arise from the different functionals used (see Figure 2). The folded structure is more stable by 0.57 eV (0.60 eV) than the unfolded one for CAM-B3LYP-D3 (B3LYP-D3) (See Table S1 in Supplementary Information). To have a more consistent picture, we rely on post HF methods such as MP2 to assess the stability at the ground state, and obtained an increased stability of the folded conformation by 0.41 eV respect to the unfolded one.

Consistent differences are observed for the optical properties, such as the one photon absorption spectra of both folded and unfolded structures. In particular, the B3LYP functional shifts the spectra by 22 nm towards the red, while CAM-B3LYP presents a less pronounced red shift of 13 nm, from 349 to 362 nm, when the unfolded structure is compared to the folded one (see Figure 3). Moreover, the transitions associated to the low energy excited states strongly vary passing from CAM-B3LYP-D to B3LYP-D. While for the unfolded conformation the former expresses the S_1 state lying at 349 nm described by a local HOMO to LUMO transition and S_2 (at 326 nm) by a local HOMO to LUMO+2 transition, the situation is different for the latter functional, with now S_1 (S_2) being described by a charge transfer HOMO to LUMO+1 (local HOMO to LUMO) transition. Results obtained by the second order Algebraic Diagrammatic Construction scheme [ADC(2)] on the ANQ fluorophore show that S_1 lies at 336 nm and is described by both local

HOMO to LUMO and HOMO-1 to LUMO+1 transitions, while S_2 lies at 320 nm with a combined charge-transfer HOMO-1 to LUMO and local HOMO-3 to LUMO transitions. This is also confirmed by the equation-of-motion coupled cluster singles and doubles calculation (EOM-CCSD) on the same ANQ part of the probe, from which S_1 , at 318 nm and S_2 at 310 nm are described by the same transitions as found from ADC(2). For this reason, and considering the wide usage of the CAM-B3LYP functional for biological applications,^{54,56,59–64} we chose to continue the analyses with this functional, combined with the dispersion term. In line with recent insights into the interpretation of optical spectra simulated with correlated methods, it can be remarked that in the case of the post-Hartree Fock methods like ADC and EOM-CC the transition vector describes one-particle excitation from one correlated state to another rather than a transition from one orbital to another in an excited Slater-determinant. For these methods, orbital depictions should thus be regarded as approximate ways to discuss transition characters.⁶⁵

When the probe is embedded in the enzyme, only the unfolded form is found and it is thus rather Figure 2(c) which provides a realistic view on ANQ-IMC-6. Since the electronic interaction of the probe with the protein environment is the focus of the current study, the optical properties of the unfolded form have been simulated using models in which the interaction with the environment can be switched on and off.

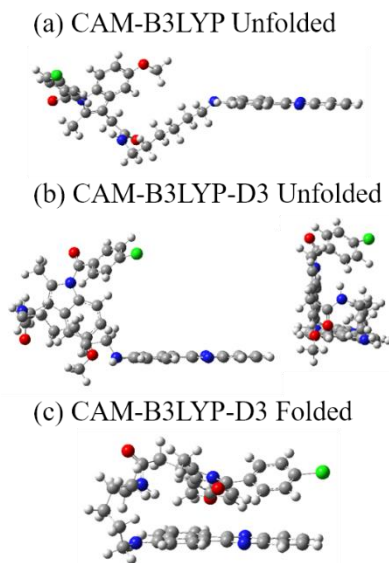


Figure 2 – Comparison between the unfolded and folded structures of the ANQ-IMC-6 probe optimized by means of the CAM-B3LYP-D functional. For case (b), two different views are proved.

Experimentally, absorption of the probe has been found to be at 457 nm in a Tris-HCL buffer with a pH of 8.0.²² Thus, we considered also the case in which the folded probe (as it is the most stable one) is immersed in water and performed Polarizable Continuum Model (PCM) calculations (see Table S2). We observed an additional redshift of 20 nm going from vacuum to water, leading to the lowest excited state found at 383 nm (see Figure S1), which suggests that explicit solvent molecules should be considered to retrieve the experimental absorption, thus validating the use of a QM/MM approach.

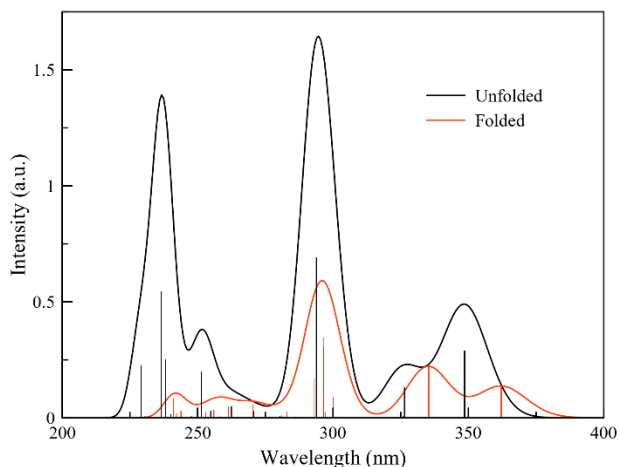


Figure 3 – Absorption spectra of ANQ-IMC-6 obtained by TDDFT/CAMB3LYP-D in vacuum. The height of vertical lines refer to the oscillator strength.

2. MD simulations

Two different MD simulations have been performed in order to assess the effect of the environment over the conformations of the probe. In the first one, the probe was immersed in a box of water molecules, in both its folded and unfolded conformations. While the folded form is stable along the simulation time and exhibits only negligible geometrical variations, the unfolded one reverts to the most stable, folded structure in less than 1 ns. On the other hand, when inserted into the protein, the steric hindrance allows only the unfolded structure to be observed. To provide a quantitative view on the conformation, the evolution of the dihedral angle between the nitrogen atoms of the probe embedded in the protein is given in Figure S2. It has a constant value in between 90° and 120°, depicting the open form. For the folded form computed in water, the same dihedral has a value of 5°.

The starting structure for the MD calculation with the protein has been obtained through docking simulations (binding energy of 12.6 kcal/mol). A detailed embedding of the probe in the enzyme from MD is given in Figure S3 and the amino acids in close proximity (i.e. at a distance smaller than 2.5 Å) have been indicated. To verify the convergence of the MD calculations, the evolution of the RMSD in time is given in Figure S4.

The MD trajectories enable a thorough look on the possible hydrogen bonds which arise between the probe and the enzyme. The -NH groups at the end of the linker act as a donor for hydrogen bond formation with the oxygen atom of the GLY654 and CYX566 aminoacids, while all the nitrogen and oxygen atoms of the probe act as acceptor for the formation of hydrogen bonds with the protein (see Table S3). Throughout the considered time window, in average there are 2.21 hydrogen bonds with the protein. The same analysis performed in water show a max distance of 0.35 nm and 30 degrees angle (N-H-O), and bear a computed average of 2.65 hydrogen bonds per time frame. Interestingly, only the -NH group of the linker close to the IMC moiety has the ability to form the bonds as donor. This is probably due to the different fluctuating nature of the IMC compared to the ANQ part (see below).

While the IMC moiety in the protein is responsible for the adhesion to the homodimer interface, the ANQ is responsible for the optical response. The flexibility of the linker in between the two parts accounts for the flexibility of the whole probe. The protein pocket in which the probe can accommodate itself is close to the edge of the monomer, resulting in the probe being located at the interface between the two monomers forming the protein structure (Figure 4). Due to this peculiar spatial position, in the surrounding of the probe some water molecules have been observed (Figure S5), which may become important in the determination of optical properties.

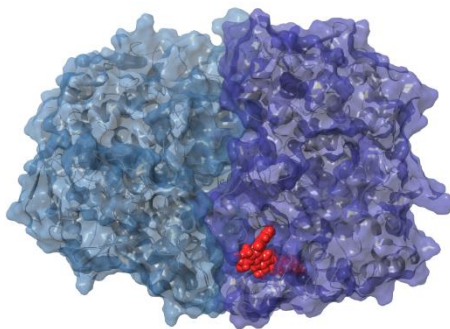


Figure 4 – Representative snapshot from the MD simulation. The probe is depicted by its van der Waals spheres (red), inserted in the pocket formed at the interface of the two proteins' monomers.

From the benchmark calculations, we know that the ground state dipole moment (D) and the transition dipole moment from the ground to the first excited state (tdm) have an almost perpendicular orientation, the previous being perpendicular to the ANQ plane and the latter oriented along ANQ's long axis. When the angle between these two vectors is computed along the MD trajectory, we observe interesting fluctuations which exhibit the flexibility of the IMC part of the probe in the protein pocket at ambient temperatures, with three major peaks at 105, 130 and 150 degrees (Figure 5). On the other hand, the angle between the tdm and the normal to the protein is much more stiff, with a peak at around 22 degrees, which enables a solid interpretation of fluorescence anisotropy experiments.

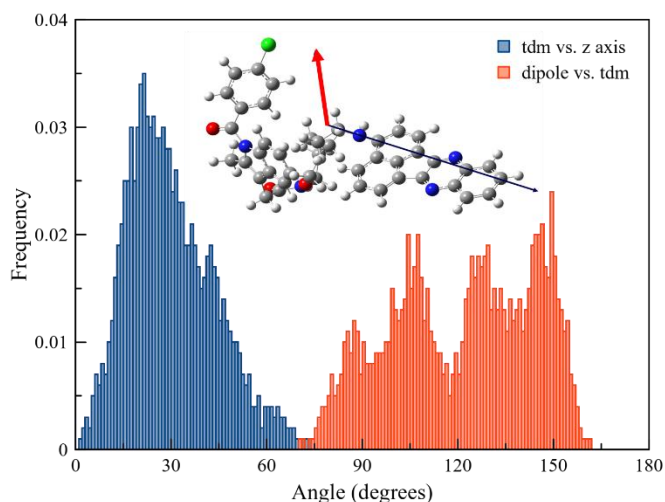


Figure 5 – Angle analysis for the probe when embedded into the protein. The dipole vector is depicted as a red arrow in the inset, while the tdm as black arrow.

The agility of the probe is herewith confirmed by the analysis of its rotational movement within the protein, which we performed by considering the rotational autocorrelation function for the transition dipole moment. It is described by an ensemble average of the second order Legendre polynomial of the angle between the absorption transition dipole at a time τ and the one at a later time $\tau+t$. In an anisotropic environment, it is often fitted by a double exponential function^{66,67}

$$C(t) = \beta_1 \exp(-t/\theta_1) + \beta_2 \exp(-t/\theta_2) + C_\infty, \quad (1)$$

with θ_1 and θ_2 the rotational correlation times. The static term C_∞ is related to the residual component of the autocorrelation function at long times, which might be significantly different from zero due to the restriction from the environment. The mean correlation time is defined as

$\langle \theta \rangle = \frac{\sum_i \beta_i \theta_i^2}{\sum_i \beta_i \theta_i}$. The results of the fit, whose quality has been checked by a reduced χ^2 analysis with a deviation of less than 10^{-5} , are given in Table 1.

Table 1 Pre-exponential parameters β and rotational correlation time θ for the probe when embedded into the protein. All rotational correlation times are given in ns.^a

	β_1	θ_1	β_2	θ_2	$C_\infty \vee$	$\langle \theta \rangle$
probe	-1.26	8.99	2.54	19.51	0.30	25.30

^a The mean correlation time $\langle \theta \rangle$ and the C_∞ parameters are also reported. Fitting time was set to 80 ns.

Being embedded in a protein, the probe experiences a rather strong steric hindrance, which is reflected in the relatively high value of the C_∞ parameter of 0.30. This agrees with the depiction in Figure 5, which shows that the overall movement of the transition dipole moment is limited throughout the time window of the MD calculation. A heavily hindered rotational decay is also visible in the high mean correlation time of 25.30 ns. The two different correlation times found are affected by the intrinsic fluorescence decay, the anisotropy of the environment and the rotational motion of the protein. In the presented method, the longer correlation time of 19.51 ns can be associated to the overall motion of the protein-probe complex. Although the shorter one of 8.99 ns might mainly exhibit characteristics of the probe itself, it still carries important influences of the motion of the COX-2 dimer.⁶⁸ As a remark and referring to our experience with fluorescent probes in lipid bilayer membranes, it can be said that the order of magnitude of both $\langle \theta \rangle$ and θ_2 are comparable to the ones found for the conformer of the widely used Laurdan probe whose location and orientation are affected the most by the stiff environment of a surrounding solid gel phase membrane at room temperature.^{54,62,69,64} This observation illustrates the power of rotational correlation analyses to investigate biological tissues and shows that these techniques can provide deeper insights into intrinsic properties which enable the comparison of different environments.

3. QM/MM analyses

(a) *One-photon absorption (OPA)*

To assess the effect of the environment on the absorption spectrum of the probe unfolded in the protein, we compare two different scenarios in which the spectra of the probe are obtained: (i) The structure of the probe is extracted from the MD simulation without consideration of the environment (labelled as OPA no enzyme); and (ii) The probe is subject to the full QM/MM approach, in which the environment has been considered as point charges (OPA enzyme). The results are reported in Figure 6.

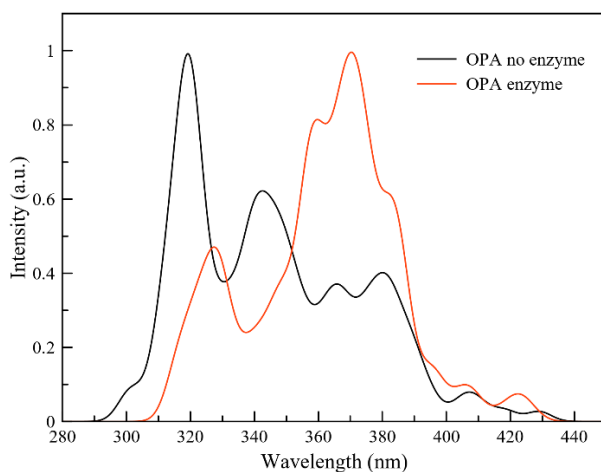


Figure 6 – One photon absorption spectra of the unfolded form of ANQ-IMC-6 probe extracted from the selected snapshots (OPA no enzyme), and of the probe’s structures extracted from the snapshots while the environment is taken into account as point charges (OPA enzyme).

The first noticeable result is the spread of the absorption when the thermal fluctuations are considered (OPA no enzyme) with a strong 80 nm redshift correlated to this effect, resulting in the S_1 absorption energy in the violet 357-429 nm window. Moreover, the presence of additional absorption bands reveals the high flexibility of the probe even when interacting with the enzyme. The addition of the environment (OPA enzyme) has only a little effect over the absorption spectrum energy, with a negligible shift in wavelengths in the 337-427 nm range, but with a strong impact in the nature of the transitions. In fact, for ‘OPA no enzyme’ the S_1 is described by a major HOMO to LUMO transition (70%) and a minor HOMO to LUMO+1 (30%) (See Table S4). The Λ diagnostic of Peach *et al.*⁷⁰, which gives a value of 0.67, confirms that these transitions possess a local character as both orbitals are localized over the ANQ moiety. When the environment is present the situation is more complex, with now two major contributions for the S_1 state, arising from HOMO to LUMO (23%) and HOMO-2 to LUMO (20%) transitions and different minor contributions (full data are reported in Table S4 in the Supporting Information). The reason behind

this striking difference can be traced back to the nature of the transitions and is reflected into the Λ diagnostic of Peach *et al.*, with now values below 0.5, (0.37 for S_1), indicating a charge transfer character for all excited states when the environment is explicitly considered, as some orbitals are now localized over the IMC moiety (see Figure S6). Interestingly, the absorption wavelength is not affected by the presence of the protein environment, suggesting that its effect is more subtle. The difference between the two approaches is due to the non-bonded interactions with elements and species from the environment. From an analysis of the probe's environment, 10 water molecules are found at a distance of less than 5 Å to the ANQ moiety, which directly affects the electronic properties of the probe. Thereupon, the protein environment generates positive regions in the vicinity of the probe, which diminishes the contribution of the local HOMO to LUMO transition at the expense of the charge transfer ones like HOMO-2 to LUMO and HOMO to LUMO+1.

The current results strongly differ from the ones discussed by Zhang *et al.*²², showing that the incorporation of the effect of the environment is indispensable when optical properties (either absorption or emission) are assessed. We thus suggest the use of more complete, albeit computationally more expensive methods, to properly assess the optical properties of probes embedded in biological environments.

This conclusion holds true even when we change the nature of the environment, from the enzyme to water, although now the effect of the conformation is also present (in water only the folded state is stable). The characteristics of the lowest excitations change, with absorption at 417 nm (see Figure S1 and Table S5) and a predominant HOMO-1 to LUMO assignment, with only a small contribution of HOMO to LUMO+1. The S_2 is a mixture of HOMO to LUMO+1 and HOMO to LUMO+2 excitations. The Peach analysis once more suggests the local character of these transitions, with values of 0.63 and 0.59, as also confirmed by the localization of the molecular orbitals (Figure S7). Especially in the orbital depictions of LUMO+1 and LUMO+2, the through-space interactions between the two parts of the folded probe are seen. These results show that a continuum or PCM model is often very different from a calculation in which the solvent molecules are explicitly taken into account; comparing the two approaches, a red shift of 34 nm is seen for the QM/MM results (Table S2). The difference lies in the nature of the calculations; per definition, in the QM/MM calculations, the quality of the obtained geometry is determined by the force field used, while for PCM the approach is entirely based on quantum chemistry. Based on this

discussion and following the overall comparison of the absorption spectra of ANQ-IMC-6 embedded in water (Figure S1) and in protein (Figure 5), it can be said that the absorption spectra are determined by the embedding environment. In our scheme, the results will be further improved if polarizable force fields are used in the MD step. Of course, methodologically, also our QM/MM scheme can be outperformed when ab initio MD is used. However, the considered time window and the dimensions of the probe as such and of the relevant surrounding protein environment warrants our approach.

(b) Two-photon absorption (TPA)

In the OPA case, the observed differences are mainly related to changes in geometry when the environment is changed, or to profound influences on the ground to excited state transition dipole moments. TPA cross section (in units of Göppert-Mayer, GM) depends as well on the transition state dipole moments in between the excited states and it is expected that the differences in the obtained spectroscopic properties increase with respect to the OPA case when the QM/MM results without/with environment are considered, since TPA is more sensitive to the presence of the environment surrounding the probe.

Since in TPA two low frequency photons are used instead of one high frequency, the TPA spectrum for the probe embedded in the COX-2 enzyme is now extending up to 850 nm, while it extends up to 880 nm when it is immersed in water (Figure S8). When these results are compared, the largest effect is due to the change in geometry since the folded form is found in aqueous environment and the L-shaped elongated one in COX-2.

When the protein is present, we observe that the S_2 excited state is the TPA active one, with cross section values increasing up to 20 GM, which is comparable to the values obtained by photoactive probes used in lipid bilayer membranes.⁶² The S_1 and S_3 have considerably smaller but similar values around 5 GM (see Figure 7). The induced effects of the environment on the optical properties is most apparent when the TPA cross sections of S_2 over the different snapshots are calculated with or without the inclusion of the embedding: when it is discarded, the cross section drops more than 5 GM (compare Figure 7 with Figure S9). An interesting effect can be seen for states S_1 and S_3 : the cross section value of the latter is comparable with the one of the former when the interactions are enabled, while a consideration of the geometries alone exhibit a clear splitting of the two TPA amplitudes with ~ 9 GM for S_3 and ~ 3 GM for S_1 . On the other hand, when the

probe is immersed in water, the S₂ state remains the most prominent one, although its cross section of 8 GM is twice smaller than the one obtained in the enzyme (see Figure S10). This effect is largely ascribed to the change in conformation of the probe. These theoretical results are corroborated by two-photon action measurements, which report a significantly higher cross section when the COX-2 enzyme is present.²²

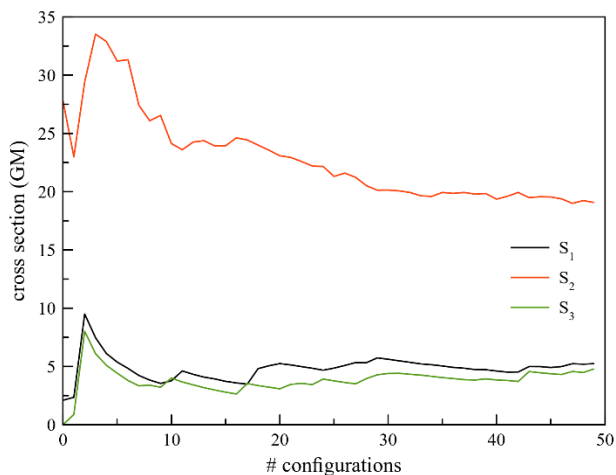


Figure 7 – Two-Photon Absorption cross sections calculated in Göppert-Mayer (GM) for the S₁, S₂ and S₃ excited states of the probe embedded in the enzyme. The results are based on the selected snapshots.

(c) *First hyperpolarizability*

Finally, we would like to address different non-linear optical properties related to the first hyperpolarizability β , namely through Hyper Rayleigh Scattering (HRS) and the Electric Field Induced Second Harmonic Generation (EFISH). In the latter technique, the main contribution is ascribed to β_{vec} , defined as the projection of β onto the ground state dipole moment μ :

$$\beta_{vec} = \frac{1}{3} \sum_{i,j} (2\beta_{iij} \mu_j + \beta_{ijj} \mu_i) \quad (2)$$

The HRS signal can be derived as $\langle \beta_{HRS} \rangle = \sqrt{\langle \beta_{ZZZ}^2 \rangle + \langle \beta_{XZZ}^2 \rangle}$, with the brackets denoting the orientational distribution average of the molecule in the environment. These averages can then be expressed as a combination of β_{ijk} tensor components in molecular frame.^{61,71}

The effect of the inclusion of the environment as point charges has a strong effect also for this analysis. In fact, β_{HRS} increases from 11×10^{-30} esu to 20×10^{-30} esu going from a QM/MM approach to include the enzyme, with an overall double enhancement of the signal. Even more

affected by the environments is β_{vec} , for which its presence boosts the signal from 6×10^{-30} esu up to 30×10^{-30} esu, with a total five times enhancement (see Figure 8). The difference between the β_{HRS} values obtained in both calculations is related to the 10 water molecules in the neighbourhood of the probe, which have a profound influence on the transition dipole moments between the excited states. The stronger increase of the β_{vec} results is the direct consequence of the influence of these polar molecules on the ground state dipole moment of the probe. The incorporation of the environment in the calculations determines thus which of the two analyses entails the largest signal. Without considering the waters and the enzyme, β_{vec} only amounts to the half of β_{HRS} , while with the probe's surrounding, the latter amounts to 66% of the value of the former. This ratio is in agreement with the attenuation found between β_{vec} and β_{HRS} in the case of molecular probes embedded in the lipophilic region of a stiff saturated lipid bilayer membrane in its solid gel phase,⁷² in which a few water molecules are still found in the neighbourhood of the probe, comparable to the present study of the ANQ-IMC-6 compound.

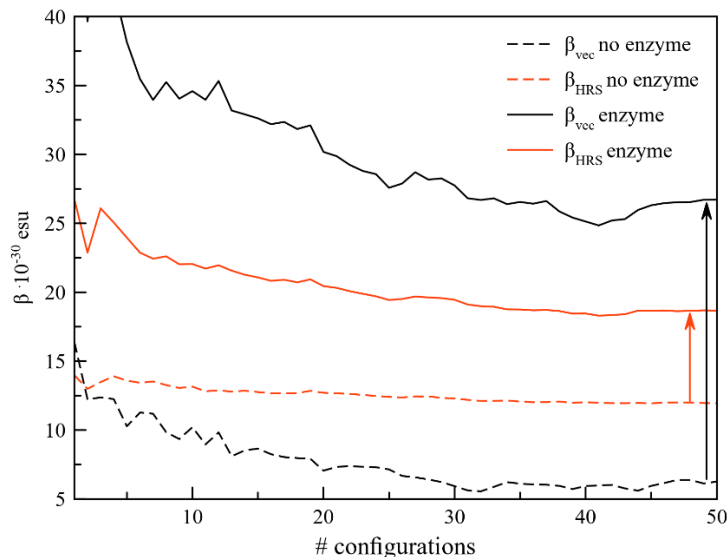


Figure 8 – β_{vec} and β_{HRS} calculated for the selected snapshots with the QM/MM method without (no enzyme) and with (enzyme) environment. Arrows depict the enhancement of the signal due to the presence of the environment.

Conclusions

By a multiscale computational approach, we have studied the (non) linear optical properties of ANQ-IMC-6 when embedded in the COX-2 enzyme. A profound benchmark allowed us to choose the proper functional to use for the subsequent analysis, resulting in the choice of the CAM-B3LYP functional as the best performing. Moreover, the addition of the Grimme's dispersion term has been proven crucial for a proper description of the investigated system.

Molecular dynamics simulations have shown the stability of the probe when inserted into the enzyme hydrophobic pocket at the interface of the homodimer, due to the presence of hydrogen bonding. Moreover, while the folded conformer is the most stable when immersed into a solvent, the unfolded conformer is stabilized in the enzyme. The analysis of the rotation ability of the probe accentuates the stiff environment of the protein. The simulated spectroscopic data point at the concerted movement of the probe and the protein together, while they also visualize the intrinsic properties of the IMC-ANQ-6 probe. It can be remarked that steric hindrance, packing and stiffness of different biological media can be compared when the exponential decay times obtained in the analyses of the rotational autocorrelation functions are evaluated.

The QM/MM analyses on OPA spectra revealed the strong effect of the presence of the environment in the shape of the absorption spectra, changing the nature of the transitions, from local when the environment is 'switched off' to a charge transfer character when the environment is explicitly considered. The TPA spectra confirm the importance of the presence of the protein environment, with a twofold enhancement of the signal when the protein is present, compared to the water case. Once more, this is evident when second-harmonic generated analyses are considered, in which a strong enhancement of the signal has been computed when the protein is explicitly considered, with up to a five time enhancement for β_{vec} .

These results show that the ANQ-IMC-6 probe possess interesting absorption properties which should not be neglected when considering its possible use as cancer diagnostic; although the experimental focus relies on its fluorescence properties, also the (non)linear absorption abilities of this probe should be taken into consideration.

Supporting information

The Supporting Information is available free of charge at doi:10.1039/xxxxxxx

Analysis of the lowest excited states of the unfolded and folded structures of ANQ-IMC-6; amino acids of COX-2 in close proximity of the probe; CHELPG charges used in the MD calculations; representative snapshot of the protein and embedded probe; frontier molecular orbitals of the probe; two-photon absorption spectrum and cross sections

Author contributions

S.O., M.M., N.A.M., S.K.: Calculations; S.O., N.A.M, S.K.: design of the project; S.O.: supervision of M.M.; S.O., S.K.: Redaction of the article

Conflicts of interests

There are no conflicts to declare.

Acknowledgements

S.O. thanks the Polish National Science Centre for funding (grant no. UMO-2018/31/D/ST4/01475). The authors acknowledge the Swedish (SNIC) and Flemish (VSC) national computer infrastructures. This research was carried out with the support of the Interdisciplinary Center for Mathematical and Computational Modeling at the University of Warsaw (ICM UW) under grant no G83-28.

References

- 1 T. Pewklang, K. Chansaenpak, R.-Y. Lai, P. Noisa and A. Kamkaew, Aza-BODIPY probe for selective visualization of cyclooxygenase-2 in cancer cells, *RSC Adv.*, 2019, **9**, 13372–13377.
- 2 M. Breinig, P. Schirmacher and M. A. Kern, Cyclooxygenase-2 (COX-2) - A therapeutic target in liver cancer?, *Curr. Pharm. Design*, 2007, **13**, 3305–3315.
- 3 K. Echizen, O. Hirose, Y. Maeda and M. Oshima, Inflammation in gastric cancer: Interplay of the COX-2/prostaglandin E-2 and Toll-like receptor/MyD88 pathways, *Cancer Sci.*, 2016, **107**, 391–397.
- 4 M. J. Edelman, L. Hodgson, X. Wang, R. A. Kratzke and E. E. Vokes, Cyclooxygenase-2 (COX-2) As a Predictive Marker for the Use of COX-2 Inhibitors in Advanced Non-Small-Cell Lung Cancer, *J. Clin. Oncol.*, 2012, **30**, 2019–2020.

- 5 H. S. Kim, A. Sharma, W. X. Ren, J. Han and J. S. Kim, COX-2 Inhibition mediated anti-angiogenic activatable prodrug potentiates cancer therapy in preclinical models, *Biomaterials*, 2018, **185**, 63–72.
- 6 M. L. Nasi and N. Castiglione, Cyclooxygenase-2 (COX-2) a new prognostic and predictive factor for ovarian cancer? Are all the criteria fulfilled?, *Ann. Oncol.*, 2002, **13**, 1169–1171.
- 7 S. Nath, L. Das Roy, P. Grover, S. Rao and P. Mukherjee, Mucin 1 Regulates Cox-2 Gene in Pancreatic Cancer, *Pancreas*, 2015, **44**, 909–917.
- 8 A. Thiel, J. Mrena and A. Ristimaki, Cyclooxygenase-2 and Gastric Cancer, *Cancer Metastasis Rev.*, 2011, **30**, 387–395.
- 9 D. Wang and R. N. DuBois, The role of COX-2 in intestinal inflammation and colorectal cancer, *Oncogene*, 2010, **29**, 781–788.
- 10 Z. Khan, N. Khan, R. P. Tiwari, N. K. Sah, G. B. K. S. Prasad and P. S. Bisen, Biology of Cox-2: An Application in Cancer Therapeutics, *Curr. Drug Targets*, 2011, **12**, 1082–1093.
- 11 R. de S. Pereira, Selective Cyclooxygenase-2 (COX-2) Inhibitors Used for Preventing or Regressing Cancer, *Recent Patents Anti-Canc. Drug Discov.*, 2009, **4**, 157–163.
- 12 E. F. J. de Vries, Imaging of cyclooxygenase-2 (COX-2) expression: Potential use in diagnosis and drug evaluation, *Curr. Pharm. Design*, 2006, **12**, 3847–3856.
- 13 J. F. Evans and S. L. Kargman, Cancer and cyclooxygenase-2 (COX-2) inhibition, *Curr. Pharm. Design*, 2004, **10**, 627–634.
- 14 K. Chansaenpak, M. Wang, S. Liu, Z. Wu, H. Yuan, P. S. Conti, Z. Li and F. P. Gabbai, Synthesis and in vivo stability studies of [F-18]-zwitterionic phosphonium aryltrifluoroborate/indomethacin conjugates, *RSC Adv.*, 2016, **6**, 23126–23133.
- 15 K. Chansaenpak, B. Vabre and F. P. Gabbai, [F-18]-Group 13 fluoride derivatives as radiotracers for positron emission tomography, *Chem. Soc. Rev.*, 2016, **45**, 954–971.
- 16 L. Milas, Cyclooxygenase-2 (COX-2) enzyme inhibitors and radiotherapy, *Am. J. Clin. Oncol.-Cancer Clin. Trials*, 2003, **26**, S66–S69.
- 17 A. Bhardwaj, J. Kaur, F. Wuest and E. E. Knaus, Fluorophore-Labeled Cyclooxygenase-2 Inhibitors for the Imaging of Cyclooxygenase-2 Overexpression in Cancer: Synthesis and Biological Studies, *ChemMedChem*, 2014, **9**, 109–116.
- 18 Y. Ti, L. Yu, Y. Tang, T. Jin, M. Yang, R. Wang, Y. Xu and W. Zhu, hypoxia-activated near infrared fluorescent probe for cyclooxygenase-2 and in vivo imaging for tumor and inflammation, *Sens. Actuator B-Chem.*, 2018, **265**, 582–590.
- 19 M. J. Uddin, B. C. Crews, A. L. Blobaum, P. J. Kingsley, D. L. Gorden, J. O. McIntyre, L. M. Matrisian, K. Subbaramaiah, A. J. Dannenberg, D. W. Piston and L. J. Marnett, Selective Visualization of Cyclooxygenase-2 in Inflammation and Cancer by Targeted Fluorescent Imaging Agents, *Cancer Res.*, 2010, **70**, 3618–3627.
- 20 M. J. Uddin, B. C. Crews, K. Ghebreselasie and L. J. Marnett, Design, Synthesis, and Structure-Activity Relationship Studies of Fluorescent Inhibitors of Cyclooxygenase-2 as Targeted Optical Imaging Agents, *Bioconjugate Chem.*, 2013, **24**, 712–723.
- 21 H. Zhang, J. Fan, J. Wang, B. Dou, F. Zhou, J. Cao, J. Qu, Z. Cao, W. Zhao and X. Peng, Fluorescence Discrimination of Cancer from Inflammation by Molecular Response to COX-2 Enzymes, *J. Am. Chem. Soc.*, 2013, **135**, 17469–17475.
- 22 H. Zhang, J. Fan, J. Wang, S. Zhang, B. Dou and X. Peng, An Off-On COX-2-Specific Fluorescent Probe: Targeting the Golgi Apparatus of Cancer Cells, *J. Am. Chem. Soc.*, 2013, **135**, 11663–11669.

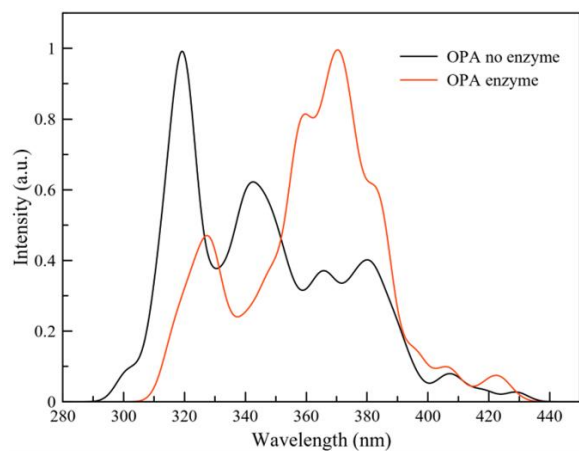
- 23 Q. Zhang, Z. Han, J. Tao, W. Zhang, P. Li, L. Tang and Y. Gu, A novel near-infrared fluorescent probe for monitoring cyclooxygenase-2 in inflammation and tumor, *J. Biophotonics*, DOI:10.1002/jbio.201700339.
- 24 Y. Chen, Design and construction of COX-2 specific fluorescent probes, *Mol. Cell. Probes*, 2019, **48**, 101472.
- 25 J. H. Jang, H. Lee, A. Sharma, S. M. Lee, T. H. Lee, C. Kang and J. S. Kim, Indomethacin-guided cancer selective prodrug conjugate activated by histone deacetylase and tumour-associated protease, *Chem. Commun.*, 2016, **52**, 9965–9968.
- 26 H. S. Kim, T. Park, W. X. Ren, J.-Y. Lim, M. Won, J. S. Heo, S. G. Lee and J. S. Kim, COX-2 targeting indomethacin conjugated fluorescent probe, *Dyes Pigment.*, 2018, **150**, 261–266.
- 27 H. Zhang, J. Fan, K. Wang, J. Li, C. Wang, Y. Nie, T. Jiang, H. Mu, X. Peng and K. Jiang, Highly Sensitive Naphthalene-Based Two-Photon Fluorescent Probe for in Situ Real-Time Bioimaging of Ultratrace Cyclooxygenase-2 in Living Biosystems, *Anal. Chem.*, 2014, **86**, 9131–9138.
- 28 B. Wang, J. Fan, X. Wang, H. Zhu, J. Wang, H. Mu and X. Peng, A Nile blue based infrared fluorescent probe: imaging tumors that over-express cyclooxygenase-2, *Chem. Commun.*, 2015, **51**, 792–795.
- 29 J. K. Dhanjal, A. K. Sreenidhi, K. Bafna, S. P. Katiyar, S. Goyal, A. Grover and D. Sundar, Computational Structure-Based De Novo Design of Hypothetical Inhibitors against the Anti-Inflammatory Target COX-2, *PLOS ONE*, 2015, **10**, e0134691.
- 30 M. I. Ortiz, E. Fernández-Martínez, L. E. Soria-Jasso, I. Lucas-Gómez, R. Villagómez-Ibarra, M. P. González-García, G. Castañeda-Hernández and M. Salinas-Caballero, Isolation, identification and molecular docking as cyclooxygenase (COX) inhibitors of the main constituents of *Matricaria chamomilla* L. extract and its synergistic interaction with diclofenac on nociception and gastric damage in rats, *Biomedicine & Pharmacotherapy*, 2016, **78**, 248–256.
- 31 C. J. Hawkey, COX-1 and COX-2 inhibitors, *Best Practice & Research Clinical Gastroenterology*, 2001, **15**, 801–820.
- 32 D. Riendeau, M. D. Percival, S. Boyce, C. Brideau, S. Charleson, W. Cromlish, D. Ethier, J. Evans, J. P. Falgoutyret, A. W. FordHutchinson, R. Gordon, G. Greig, M. Gresser, J. Guay, S. Kargman, S. Leger, J. A. Mancini, G. O'Neill, M. Ouellet, I. W. Rodger, M. Therien, Z. Wang, J. K. Webb, E. Wong, L. Xu, R. N. Young, R. Zamboni, P. Prasit and C. C. Chan, Biochemical and pharmacological profile of a tetrasubstituted furanone as a highly selective COX-2 inhibitor, *Br. J. Pharmacol.*, 1997, **121**, 105–117.
- 33 A. A. Khan, M. Iadarola, H.-Y. T. Yang and R. A. Dionne, Expression of COX-1 and COX-2 in a Clinical Model of Acute Inflammation, *The Journal of Pain*, 2007, **8**, 349–354.
- 34 A. K. Upadhyay, J. R. Horton, X. Zhang and X. Cheng, Coordinated methyl-lysine erasure: structural and functional linkage of a Jumonji demethylase domain and a reader domain, *Current Opinion in Structural Biology*, 2011, **21**, 750–760.
- 35 A. D. Becke, Density-functional thermochemistry. III. The role of exact exchange, *The Journal of Chemical Physics*, 1993, **98**, 5648–5652.
- 36 C. Lee, W. Yang and R. G. Parr, Development of the Colle-Salvetti correlation-energy formula into a functional of the electron density, *Phys. Rev. B*, 1988, **37**, 785–789.
- 37 T. Yanai, D. P. Tew and N. C. Handy, A new hybrid exchange-correlation functional using the Coulomb-attenuating method (CAM-B3LYP), *Chem. Phys. Lett.*, 2004, **393**, 51–57.

- 38 T. Dunning, Gaussian-Basis Sets for Use in Correlated Molecular Calculations .1. the Atoms Boron Through Neon and Hydrogen, *J. Chem. Phys.*, 1989, **90**, 1007–1023.
- 39 M. J. Frisch, G. W. Trucks, H. B. Schlegel, G. E. Scuseria, M. A. Robb, J. R. Cheeseman, G. Scalmani, V. Barone, G. A. Petersson, H. Nakatsuji, X. Li, M. Caricato, A. V. Marenich, J. Bloino, B. G. Janesko, R. Gomperts, B. Mennucci, H. P. Hratchian, J. V. Ortiz, A. F. Izmaylov, J. L. Sonnenberg, Williams, F. Ding, F. Lipparini, F. Egidi, J. Goings, B. Peng, A. Petrone, T. Henderson, D. Ranasinghe, V. G. Zakrzewski, J. Gao, N. Rega, G. Zheng, W. Liang, M. Hada, M. Ehara, K. Toyota, R. Fukuda, J. Hasegawa, M. Ishida, T. Nakajima, Y. Honda, O. Kitao, H. Nakai, T. Vreven, K. Throssell, J. A. Montgomery Jr., J. E. Peralta, F. Ogliaro, M. J. Bearpark, J. J. Heyd, E. N. Brothers, K. N. Kudin, V. N. Staroverov, T. A. Keith, R. Kobayashi, J. Normand, K. Raghavachari, A. P. Rendell, J. C. Burant, S. S. Iyengar, J. Tomasi, M. Cossi, J. M. Millam, M. Klene, C. Adamo, R. Cammi, J. W. Ochterski, R. L. Martin, K. Morokuma, O. Farkas, J. B. Foresman and D. J. Fox, *Gaussian 16 Rev. C.01*, Wallingford, CT, 2016.
- 40 S. Grimme, J. Antony, S. Ehrlich and H. Krieg, A consistent and accurate ab initio parametrization of density functional dispersion correction (DFT-D) for the 94 elements H-Pu, *The Journal of Chemical Physics*, 2010, **132**, 154104.
- 41 J. Schirmer, *Phys. Rev. A*, 1982, **26**, 2395–2416.
- 42 A. Dreuw and M. Wormit, The algebraic diagrammatic construction scheme for the polarization propagator for the calculation of excited states, *Wiley Interdiscip. Rev.-Comput. Mol. Sci.*, 2015, **5**, 82–95.
- 43 M. Wormit, D. R. Rehn, P. H. P. Harbach, J. Wenzel, C. M. Krauter, E. Epifanovsky and A. Dreuw, *Mol. Phys.*, 2014, **112**, 774.
- 44 J. F. Stanton and R. J. Bartlett, The equation of motion coupled-cluster method. A systematic biorthogonal approach to molecular excitation energies, transition probabilities, and excited state properties, *J. Chem. Phys.*, 1993, **98**, 7029–7039.
- 45 E. Epifanovsky, D. Zuev, X. Feng, K. Khistyayev, Y. Shao and A. I. Krylov, General implementation of the resolution-of-the-identity and Cholesky representations of electron repulsion integrals within coupled-cluster and equation-of-motion methods: Theory and benchmarks, *J. Chem. Phys.*, 2013, **139**, 134105.
- 46 Y. Shao, Z. Gan, E. Epifanovsky, A. T. B. Gilbert, M. Wormit, J. Kussmann, A. W. Lange, A. Behn, J. Deng, X. Feng, D. Ghosh, M. Goldey, P. R. Horn, L. D. Jacobson, I. Kaliman, R. Z. Khaliullin, T. Kus, A. Landau, J. Liu, E. I. Proynov, Y. M. Rhee, R. M. Richard, M. A. Rohrdanz, R. P. Steele, E. J. Sundstrom, H. L. Woodcock, P. M. Zimmerman, D. Zuev, B. Albrecht, E. Alguire, B. Austin, G. J. O. Beran, Y. A. Bernard, E. Berquist, K. Brandhorst, K. B. Bravaya, S. T. Brown, D. Casanova, C.-M. Chang, Y. Chen, S. H. Chien, K. D. Closser, D. L. Crittenden, M. Diedenhofen, R. A. DiStasio, H. Do, A. D. Dutoi, R. G. Edgar, S. Fatehi, L. Fusti-Molnar, A. Ghysels, A. Golubeva-Zadorozhnaya, J. Gomes, M. W. D. Hanson-Heine, P. H. P. Harbach, A. W. Hauser, E. G. Hohenstein, Z. C. Holden, T.-C. Jagau, H. Ji, B. Kaduk, K. Khistyayev, J. Kim, J. Kim, R. A. King, P. Klunzinger, D. Kosenkov, T. Kowalczyk, C. M. Krauter, K. U. Lao, A. D. Laurent, K. V. Lawler, S. V. Levchenko, C. Y. Lin, F. Liu, E. Livshits, R. C. Lochan, A. Luenser, P. Manohar, S. F. Manzer, S.-P. Mao, N. Mardirossian, A. V. Marenich, S. A. Maurer, N. J. Mayhall, E. Neuscamman, C. M. Oana, R. Olivares-Amaya, D. P. O’Neill, J. A. Parkhill, T. M. Perrine, R. Peverati, A. Prociuk, D. R. Rehn, E. Rosta, N. J. Russ, S. M. Sharada, S. Sharma, D. W. Small, A. Sodt, T. Stein, D. Stueck, Y.-C. Su, A. J. W. Thom, T. Tsuchimochi, V. Vanovschi, L. Vogt, O. Vydrov, T. Wang, M. A. Watson, J.

- Wenzel, A. White, C. F. Williams, J. Yang, S. Yeganeh, S. R. Yost, Z.-Q. You, I. Y. Zhang, X. Zhang, Y. Zhao, B. R. Brooks, G. K. L. Chan, D. M. Chipman, C. J. Cramer, W. A. Goddard, M. S. Gordon, W. J. Hehre, A. Klamt, H. F. Schaefer, M. W. Schmidt, C. D. Sherrill, D. G. Truhlar, A. Warshel, X. Xu, A. Aspuru-Guzik, R. Baer, A. T. Bell, N. A. Besley, J.-D. Chai, A. Dreuw, B. D. Dunietz, T. R. Furlani, S. R. Gwaltney, C.-P. Hsu, Y. Jung, J. Kong, D. S. Lambrecht, W. Liang, C. Ochsenfeld, V. A. Rassolov, L. V. Slipchenko, J. E. Subotnik, T. Van Voorhis, J. M. Herbert, A. I. Krylov, P. M. W. Gill and M. Head-Gordon, Advances in molecular quantum chemistry contained in the Q-Chem 4 program package, *Mol. Phys.*, 2015, **113**, 184–215.
- 47 C. M. Breneman and K. B. Wiberg, *J. Comp. Chem.*, 1990, **11**, 361.
- 48 G. M. Morris, R. Huey, W. Lindstrom, M. F. Sanner, R. K. Belew, D. S. Goodsell and A. J. Olson, AutoDock4 and AutoDockTools4: Automated Docking with Selective Receptor Flexibility, *J Comput Chem*, 2009, **30**, 2785–2791.
- 49 V. Hornak, R. Abel, A. Okur, B. Strockbine, A. Roitberg and C. Simmerling, Comparison of multiple Amber force fields and development of improved protein backbone parameters, *Proteins*, 2006, **65**, 712–725.
- 50 M. J. Abraham, T. Murtola, R. Schulz, S. Páll, J. C. Smith, B. Hess and E. Lindahl, GROMACS: High performance molecular simulations through multi-level parallelism from laptops to supercomputers, *SoftwareX*, 2015, **1–2**, 19–25.
- 51 K. Aidas, C. Angeli, K. L. Bak, V. Bakken, R. Bast, L. Boman, O. Christiansen, R. Cimiraglia, S. Coriani, P. Dahle, E. K. Dalskov, U. Ekstrom, T. Enevoldsen, J. J. Eriksen, P. Ettenhuber, B. Fernandez, L. Ferrighi, H. Fliegl, L. Frediani, K. Hald, A. Halkier, C. Hattig, H. Heiberg, T. Helgaker, A. C. Hennum, H. Hettema, E. Hjertenaes, S. Host, I.-M. Hoyvik, M. F. Iozzi, B. Jansik, H. J. A. Jensen, D. Jonsson, P. Jorgensen, J. Kauczor, S. Kirpekar, T. Kjrgaard, W. Klopper, S. Knecht, R. Kobayashi, H. Koch, J. Kongsted, A. Krapp, K. Kristensen, A. Ligabue, O. B. Lutnaes, J. I. Melo, K. V. Mikkelsen, R. H. Myhre, C. Neiss, C. B. Nielsen, P. Norman, J. Olsen, J. M. H. Olsen, A. Osted, M. J. Packer, F. Pawłowski, T. B. Pedersen, P. F. Provasi, S. Reine, Z. Rinkevicius, T. A. Ruden, K. Ruud, V. V. Rybkin, P. Salek, C. C. M. Samson, A. S. de Meras, T. Saue, S. P. A. Sauer, B. Schimmelpfennig, K. Sneskov, A. H. Steindal, K. O. Sylvester-Hvid, P. R. Taylor, A. M. Teale, E. I. Tellgren, D. P. Tew, A. J. Thorvaldsen, L. Thogersen, O. Vahtras, M. A. Watson, D. J. D. Wilson, M. Ziolkowski and H. Agren, The Dalton quantum chemistry program system, *Wiley Interdiscip. Rev.-Comput. Mol. Sci.*, 2014, **4**, 269–284.
- 52 S. Grimme, A. Hansen, J. G. Brandenburg and C. Bannwarth, Dispersion-Corrected Mean-Field Electronic Structure Methods, *Chem. Rev.*, 2016, **116**, 5105–5154.
- 53 R. Sarkar, M. Boggio-Pasqua, P.-F. Loos and D. Jacquemin, Benchmarking TD-DFT and Wave Function Methods for Oscillator Strengths and Excited-State Dipole Moments, *J. Chem. Theory Comput.*, 2021, **17**, 1117–1132.
- 54 S. Osella, N. A. Murugan, N. K. Jena and S. Knippenberg, Investigation into Biological Environments through (Non)linear Optics: A Multiscale Study of Laurdan Derivatives, *J. Chem. Theory Comput.*, 2016, **12**, 6169–6181.
- 55 M. Paloncova, G. Aniander, E. Larsson and S. Knippenberg, Cyanine dyes with tail length asymmetry enhance photoselection: A multiscale study on DiD probes in a liquid disordered membrane, *Spectroc. Acta Pt. A-Molec. Biomolec. Spectr.*, 2020, **224**, 117329.

- 56S. Knippenberg and S. Osella, Push/Pull Effect as Driving Force for Different Optical Responses of Azobenzene in a Biological Environment, *J. Phys. Chem. C*, 2020, **124**, 8310–8322.
- 57M. Paloncýová, J. Tornmalm, S. Sen, J. Piguet, J. Widengren and S. Knippenberg, Photoisomerization of DiD: Molecular Dynamics Calculations Reveal the Influence of Tail Lengths, *J. Phys. Chem. C*, 2020, **124**, 5829–5837.
- 58S. Osella, M. Paloncýova, M. Sahi and S. Knippenberg, Influence of Membrane Phase on the Optical Properties of DPH, *Molecules*, 2020, **25**, 4264.
- 59S. Osella, M. Paloncýova, M. Sahi and S. Knippenberg, Influence of Membrane Phase on the Optical Properties of DPH, *Molecules*, 2020, **25**, 4264.
- 60S. Osella and S. Knippenberg, Triggering On/Off States of Photoswitchable Probes in Biological Environments, *J. Am. Chem. Soc.*, 2017, 4418–4428.
- 61S. Osella, F. Di Meo, N. A. Murugan, G. Fabre, M. Ameloot, P. Trouillas and S. Knippenberg, Combining (Non)linear Optical and Fluorescence Analysis of DiD To Enhance Lipid Phase Recognition, *J. Chem. Theory Comput.*, 2018, **14**, 5350–5359.
- 62S. Osella and S. Knippenberg, Laurdan as a Molecular Rotor in Biological Environments, *ACS Appl. Bio Mater.*, 2019, **2**, 5769–5778.
- 63M. Paloncýová, G. Anlander, E. Larsson and S. Knippenberg, Cyanine dyes with tail length asymmetry enhance photoselection: A multiscale study on DiD probes in a liquid disordered membrane, *Spectrochimica Acta Part A: Molecular and Biomolecular Spectroscopy*, 2020, **224**, 117329.
- 64S. Osella and S. Knippenberg, The influence of lipid membranes on fluorescent probes' optical properties, *Biochimica et Biophysica Acta (BBA) - Biomembranes*, 2020, 183494.
- 65S. A. Mewes and A. Dreuw, Density-based descriptors and exciton analyses for visualizing and understanding the electronic structure of excited states, *Phys. Chem. Chem. Phys.*, 2019, **21**, 2843–2856.
- 66M. Ameloot, H. Hendrickx, W. Herreman, H. Pottel, F. Vancauwelaert and W. Vandermeer, Effect of Orientational Order on the Decay of the Fluorescence Anisotropy in Membrane Suspensions - Experimental-Verification on Unilamellar Vesicles and Lipid Alpha-Lactalbumin Complexes, *Biophys. J.*, 1984, **46**, 525–539.
- 67M. Ameloot, M. vandeVen, A. U. Acuña and B. Valeur, Fluorescence anisotropy measurements in solution: Methods and reference materials (IUPAC Technical Report), *Pure and Applied Chemistry*, 2013, **85**, 589–608.
- 68Lakowicz, *Principles of Fluorescence Spectroscopy*, Springer, 3rd edition., 2007.
- 69S. Osella, N. Smisdom, M. Ameloot and S. Knippenberg, Conformational Changes as Driving Force for Phase Recognition: The Case of Laurdan, *Langmuir*, 2019, **35**, 11471–11481.
- 70M. J. G. Peach, P. Benfield, T. Helgaker and D. J. Tozer, Excitation energies in density functional theory: An evaluation and a diagnostic test, *The Journal of Chemical Physics*, 2008, **128**, 044118.
- 71Z. Hu, J. Autschbach and L. Jensen, Simulation of resonance hyper-Rayleigh scattering of molecules and metal clusters using a time-dependent density functional theory approach, *J. Chem. Phys.*, 2014, **141**, 124305.
- 72S. Knippenberg, G. Fabre, S. Osella, F. Di Meo, M. Paloncýova, M. Ameloot and P. Trouillas, Atomistic Picture of Fluorescent Probes with Hydrocarbon Tails in Lipid Bilayer Membranes: An Investigation of Selective Affinities and Fluorescent Anisotropies in Different Environmental Phases, *Langmuir*, 2018, **34**, 9072–9084.

Table of contents



Switch environment on/off

